Available online at website: https://journal.bcrec.id/index.php/bcrec

Bulletin of Chemical Reaction Engineering & Catalysis, 20 (4) 2025, 694-708

Original Research Article

Effect of Aluminium Loading on SiO_2/Al_2O_3-NiMo Catalysts Synthesized via KHP-template for Crude Palm Oil Hydrocracking

Hasanudin Hasanudin[1]*, Mhika Nakashima[1], Wan Ryan Asri[2], Novia Novia[3], Fitri Hadiah[3], Roni Maryana[4], Muhammad Al Muttaqii[4], Nino Rinaldi[4]

[1]Department of Chemistry, Faculty of Mathematics and Natural Science, Universitas Sriwijaya, Indralaya, Sumatra Selatan 30662, Indonesia.
[2]Chemistry Department, King Fahd University of Petroleum and Minerals, Dhahran 31261, Saudi Arabia.
[3]Department of Chemical Engineering, Faculty of Engineering, Universitas Sriwijaya, Indralaya, Sumatra Selatan 30662, Indonesia.
[4]Research Center for Chemistry, Indonesian Institute of Sciences, Building 452 Kawasan PUSPIPTEK, Serpong, Tangerang Selatan, Banten, Indonesia.

Received: 6th September 2025; Revised: 7th October 2025; Accepted: 7th October 2025
Available online: 13th October 2025; Published regularly: December 2025

Abstract

The present study evaluates the catalytic activity of SiO_2/Al_2O_3–x and SiO_2/Al_2O_3–x–NiMo (where x = 5, 10, 25 g of aluminium weight) synthesized using a potassium hydrogen phthalate (KHP) template-assisted route for the hydrocracking of crude palm oil (CPO) into biofuels. Increasing Al weight modified acidity, porosity, and NiMo dispersion, leading to distinct catalytic behavior. The optimal SiO_2/Al_2O_3–x–NiMo catalyst (10 g Al) achieved ~94% conversion, dominated by jet fuel-range hydrocarbons (C_{10}-C_{14}) through synergistic hydrodeoxygenation and acid-catalyzed cracking-isomerization pathway. The enhanced performance originates from the balance between acidity and metal dispersion, highlighting that both template selection and Al loading govern the design of efficient SiO_2/Al_2O_3–NiMo catalysts for biofuel production.

Keywords: SiO_2/Al_2O_3; potassium hydrogen phthalate; crude palm oil; hydrocracking; NiMo catalyst

How to Cite: Hasanudin, H., Nakashima, M., Asri, W. R., Novia, N., Hadiah, F., Maryana, R., Al Muttaqii, M., Rinaldi, N. (2025). Effect of Aluminium Loading on SiO_2/Al_2O_3-NiMo Catalysts Synthesized via KHP-template for Crude Palm Oil Hydrocracking. *Bulletin of Chemical Reaction Engineering & Catalysis*, 20 (4), 694-708. (doi: 10.9767/bcrec.20483)

Permalink/DOI: https://doi.org/10.9767/bcrec.20483

Supporting Information (SI): https://journal.bcrec.id/index.php/bcrec/article/downloadSuppFile/20483/5896

1. Introduction

The hydrocracking process is a well-established method in petroleum refining that converts heavy hydrocarbons into lighter, value-added fuels such as gasoline, diesel, and petrol [1]. Increasing energy demand and depletion of fossil resources have driven interest in biofuels as sustainable alternatives [2]. Among various conversion routes, biomass hydrocracking offers advantages such as lower operation temperatures, reduced energy consumption, and flexibility in feedstocks utilization compared with pyrolysis or transesterification [3]. Various feedstocks, including waste palm oil, algae oil, jatropha oil, and rubber seed oil, have been investigated for biofuel production under different catalysts and reaction conditions [4-9]. Among these, crude palm oil (CPO) and its derivatives are considered particularly potential feedstocks, as they possess low cost and the highest yield per hectare compared to other vegetable oils in Southeast

* Corresponding Author.
Email: hasanudin@mipa.unsri.ac.id (H. Hasanudin)

Asia, and provide high content of long-chain hydrocarbons [10].

The development of hydrocracking catalysts is of great importance in industrial processes, as they facilitate cleaner fuels production, enable compliance with environmental standards and simultaneously preserve profitable and efficient processes. Although the choice of feedstocks and reaction conditions is important, catalysts play a critical role in enhancing hydrocracking performance [11]. Typically, noble metals such as Pt and Pd are often employed as active metals for hydrocracking process due to their excellent catalytic activity. These catalysts, however, are not economical due to their high cost and proneness to deactivation and poisoning, thus limiting their industrial viability [12,13]. The use of bifunctional catalysts is commonly employed, in which acidic supports facilitate C–C cracking, whilst the active metals promote the hydrogenation–dehydrogenation reaction, have been extensively studied for their ability to control the selectivity and activity of hydrocracking process [14].

Currently, several types of bifunctional catalysts, including NiW/ZSM-5 zeolite [15], NiO–CdO/biochar [[5], Rh/HZSM-5 [16], SiO_2/Zr [17], Pd/Al_2O_3 and PdFe/Al_2O_3 [10], have been utilized for hydrocracking of palm oil-based feedstocks. In the context of bifunctional catalysts, the support must have adequate pore diameter to enhance metal dispersion and pore diffusion, sufficient acidity to perform the cracking of feedstocks, and optimal dispersion of active metals [18]. SiO_2/Al_2O_3 is one of the promising support catalysts due to its flexibility, as its acidity and textural features can be favorably tuned. This support has also been utilized for hydroprocessing-related applications [19-23]. The acid center is proposed to arise from the isomorphous substitution of Si^{4+} by Al^{3+} in the lattice of silica, which may result from diffusion of aluminium into the silica framework during high heat treatment [24]. Moreover, its textural features can be tailored using a template-assisted method, where the type of templating agent influences pore formation upon calcination [25]. Dispersing transition metals on SiO_2/Al_2O_3 may generate new surface species that develop new acid centers and enhance their acidity features. It has been reported that transition metals such as bimetallic NiMo possess comparable catalytic activity to noble metal-based systems due to synergistic features within the NiMo phase, where Mo crystals are well-dispersed and decorated with Ni as a promoter [26]. This system has been widely employed as an active metal on various supports for diverse applications [19.20.27-32], highlighting its relevance and robust performance in hydroprocessing/ hydrotreating-related applications.

Despite extensive studies on SiO_2/Al_2O_3–NiMo catalysts, their application in CPO hydrocracking and systematic investigations on tuning acidity, structural, and textural features remain limited. A previous study [33], used EDTA as a template agent, demonstrating its influence on catalyst characteristics. Herein, we introduce potassium hydrogen phthalate (KHP) as an alternative template agent, aiming to induce different pore formation characteristics and enhance catalytic performance. Although the fundamental composition of SiO_2/Al_2O_3 remains unchanged, the choice of template significantly impacts the catalyst's structural, textural, and acidic properties, as well as metal dispersion upon NiMo loading. The use of template agent KHP in SiO_2/Al_2O_3–NiMo outperformed EDTA in terms of higher acidity value, higher BET surface area, pore volume, and average pore diameter. These modifications ultimately lead to distinct catalytic features in CPO hydrocracking, highlighting the role of the template method in tailoring catalyst performance. The objective of this study is therefore to investigate how aluminium loading affects the properties and catalytic performance of KHP-templated SiO_2/Al_2O_3–NiMo catalysts in crude palm oil hydrocracking.

2. Materials and Methods

2.1 Materials

Tetraethyl orthosilicate (TEOS, Sigma-Aldrich) and aluminium nitrate nonahydrate ($Al(NO_3)_3 \cdot 9H_2O$, Sigma-Aldrich) were used as silica and aluminium precursors, respectively. Nickel(II) chloride hexahydrate ($NiCl_2 \cdot 6H_2O$, Sigma-Aldrich) and ammonium molybdate tetrahydrate ($(NH_4)_2MoO_4 \cdot 4H_2O$, Sigma-Aldrich) were used as NiMo precursors, while potassium hydrogen phthalate (KHP, Sigma-Aldrich) was used as the templating agent. Additional reagents included ammonium hydroxide solution (25%, Sigma-Aldrich), and ethanol (≥99.5, Sigma-Aldrich).

2.2 Preparation of SiO_2/Al_2O_3 using KHP Template-assisted Method with Varying Aluminium Weights

A 5% (w/v) potassium hydrogen phthalate (KHP) solution was prepared by dissolving 5 g of KHP in 100 mL of deionized water. In a typical synthesis, 100 mL of tetraethyl orthosilicate (TEOS) was dissolved in 200 mL of ethanol and stirred at room temperature for 15 min. A series of $Al(NO_3)_3 \cdot 9H_2O$ powders (5, 10, and 25 g) were then dissolved in 100 mL of the KHP solution under stirring for 30 min. The mixture was combined with the TEOS–ethanol solution and stirred for 3 h. Subsequently, 10 mL of 25% NH_4OH solution was added dropwise (one drop

every 5 s) to induce gelation. The gel was aged at room temperature for 30 min, heated at 50 ˚C to form a paste, dried at 100 ˚C for 24 h, and calcined at 750 ˚C for 6 h. The resulting powders with different Al weights of 5, 10, and 25 g are denoted as SiO_2/Al_2O_3–A, SiO_2/Al_2O_3–B, SiO_2/Al_2O_3–C, respectively.

2.3 Synthesis of SiO_2/Al_2O_3–NiMo

For NiMo impregnation, 5.06 g of $NiCl_2 \cdot 6H_2O$ and 5.26 g of $(NH_4)_2MoO_4 \cdot 4H_2O$ was each dissolved in 100 mL of deionized water, mixed, and stirred for 15 min. The SiO_2/Al_2O_3 supports with different Al weight (5, 10, 25 g) were added to the mixed solution and stirred for 15 min. The slurry was heated to ~60–80 ˚C to form a paste, dried at ~100–110 ˚C for 24 h, calcined at ~750 ˚C for 6 h, and finally reduced to 350 ˚C for 2 h under H_2 flow. The resulting catalysts of SiO_2/Al_2O_3–NiMo with different Al weights of 5, 10, and 25 g are denoted as SiO_2/Al_2O_3–A–NiMo, SiO_2/Al_2O_3–B–NiMo, SiO_2/Al_2O_3–C–NiMo, respectively.

2.4 Characterization of Catalysts

The structural features of catalyst were examined using X'Pert Powder Diffractometer (PANalytical), operated at 40 kV and 15 mA with Cu–Kα radiation source. The diffraction patterns were scanned from 5–85˚ with a step size of 0.217˚. Infrared spectra were recorded using an IR spectrometer (Bruker Tensor II) to assess the functional groups of catalysts. Autochem II Micromeritics was used to perform NH_3–TPD. The ambient temperature in the instrument was 40 ˚C. The catalyst (~0.05 g) was pretreated at 350 ˚C for 60 min under an inert gas (5% in He, v/v) with a gas flow rate of 50 $mL.min^{-1}$. Prior to desorption, He gas was flowed for purging at 100 ˚C. The adsorption of NH_3 was carried out at 100 ˚C for 30 min, whereas the desorption of NH_3 was performed at 100 ˚C to 800˚ with a heating rate of 10 $˚C.min^{-1}$ and hold for 30 min. N_2 adsorption–desorption (at −196 ˚C) was performed using Nova Quantachrome. The catalyst was outgassed at 250 ˚C for 3 h. The multipoint BET was utilized to measure the surface area, whereas the BJH desorption was used to describe the pore size distribution of catalysts. Horiba LA–960 was utilized to analyze the particle size distribution. The average particle size in µm was reported with 3 repeated measurements. The surface morphology and elemental mapping of catalyst were recorded using SEM (JSM–IT00A/LA, JEOL) with acceleration voltage of 20.00 kV. The GC–MS (Agilent) equipped with HP-5MS 5% phenyl methyl silox phase capillary column was utilized to analyze the liquid product.

2.5 Hydrocracking of CPO

The catalytic activity of SiO_2/Al_2O_3–NiMo was evaluated through hydrocracking of CPO. The hydrocracking of CPO was conducted at 350 ˚C for 2 h under batch reactor. In a typical run, 20 g of CPO and 0.6 g of catalyst were mixed into the reactor and stirred at 1500 rpm. The reactor was pressurized with 20 bars of H_2, purged three times to remove unwanted gases and maintained under H_2 atmosphere during the reaction. Upon completing the hydrocracking reaction, the liquid product was collected and analyzed by GC–MS. The CPO feed showed a fatty acid (FA) pool dominated by C14:0, C16:0, C18:2, C18:1, and C18:0, which accounted for 77.33 area% of the TIC. The catalytic conversion of CPO was estimated from the disappearance of this FA pool based on the equations as follows (1):

$$Conversion\ (\%) = \left(1 - \frac{\sum \text{fatty acid}_{\text{product}}}{\sum \text{fatty acid}_{\text{feed}}}\right) \times 100\% \quad (1)$$

where, $\sum \text{fatty acid}_{\text{product}}$ and $\sum \text{fatty acid}_{\text{feed}}$ represent the summed normalized area% of the identified FA-TMS derivatives in the feed and the product respectively. For catalytic performance analysis, the GC-MS data were further classified by carbon number range to approximate fuel fractions: C_5-C_9 (gasoline range), C_{10}-C_{14} (jet range), and C_{15}-C_{22} (diesel range). In parallel, the detected compounds were grouped into four chemical classes: aromatic hydrocarbon, paraffins (n-alkenes and cyclics), branched iso-paraffins, and oxygenated species (fatty acids, alcohols, and esters), and their semi-quantitative normalized TIC area% was reported as the apparent product composition.

3. Results and Discussion

3.1 Catalyst Characterizations

The XRD diffractograms of SiO_2/Al_2O_3 and SiO_2/Al_2O_3–NiMo with varying aluminium weights are shown in Figure 1a-b. Broad peaks around $2\theta \approx 20^{\circ}$ were observed in all SiO_2/Al_2O_3 supports, corresponding to the amorphous silica–alumina lacking long-range order [24]. Compared with the EDTA-templated method reported previously [33], the absence of ordered phases of well-defined alumina reflections at low aluminium content (SiO_2/Al_2O_3–A) indicates that using KHP as the template favors an amorphous SiO_2/Al_2O_3 framework. Notably, increasing aluminium weight from 5 to 10 g (SiO_2/Al_2O_3-B) produced a slight shift of the amorphous peak to higher 2θ, where a pronounced shift was observed at 25 g (SiO_2/Al_2O_3-C), suggesting shorter interatomic distances and stronger Si–O–Al interactions. The overall amorphous features intensity decreased with aluminium weight,

which can arise from increased structural disorder in the mixed oxide [34] and stronger silica–alumina interaction.

After NiMo loading (Figure 1b), weak reflections at 2θ = 23.89, 25.33, 26.72, 32.54, 41.15, 47.41, 48.36, and 50.47° are attributed to the MoO_3 monoclinic phase (ICDD No. 00-047-1081) [35]. Another set of diffraction patterns at 2θ = 14.31, 16.12, 18.97, 28.78, 31.28, 32.82, 38.70, and 43.80° correspond to the α-$NiMoO_4$ monoclinic phase (JCPDS No. 31-0902) [36], both confirming successful deposition of NiMo species. The relative intensity of these reflections decreases with increasing aluminium weight (SiO_2/Al_2O_3–C–NiMo < SiO_2/Al_2O_3–B–NiMo < SiO_2/Al_2O_3–A–NiMo, consistent with improved dispersion at higher Al content. A concurrent reduction in the intensity of the broad feature near 2θ = 21.81° with increasing aluminium in the NiMo–loaded samples indicate disruption of crystalline ordering within the deposited phases. Overall, the XRD results suggest that increasing aluminium weight in SiO_2/Al_2O_3 enhances NiMo dispersion.

FTIR spectra (Figure 1c) show a strong band at ~1072 cm^{-1} (Si–O–Si asymmetric stretching) and a shoulder near ~1200 cm^{-1} (external SiO_4 linkage) in SiO_2/Al_2O_3–A [25,37]. With increasing aluminium weight, the ~1072 cm^{-1} band shifts to lower wavenumber and the shoulder weakens, indicating increased framework disorder and greater Si–O–Al formation [38]. The ~796 cm^{-1} Si–O–Si bending band also decreases with aluminium weight, consistent with substitution by Si–O–Al bonds [39,40].

Upon NiMo loading, additional features appear: ~614 cm^{-1} (Ni–O), ~673 cm^{-1} (Mo–O–Mo), and ~958 cm^{-1} (Mo=O), and a weak band at 934 cm^{-1} corresponds to Mo–O–Si/Mo–O–Al linkages

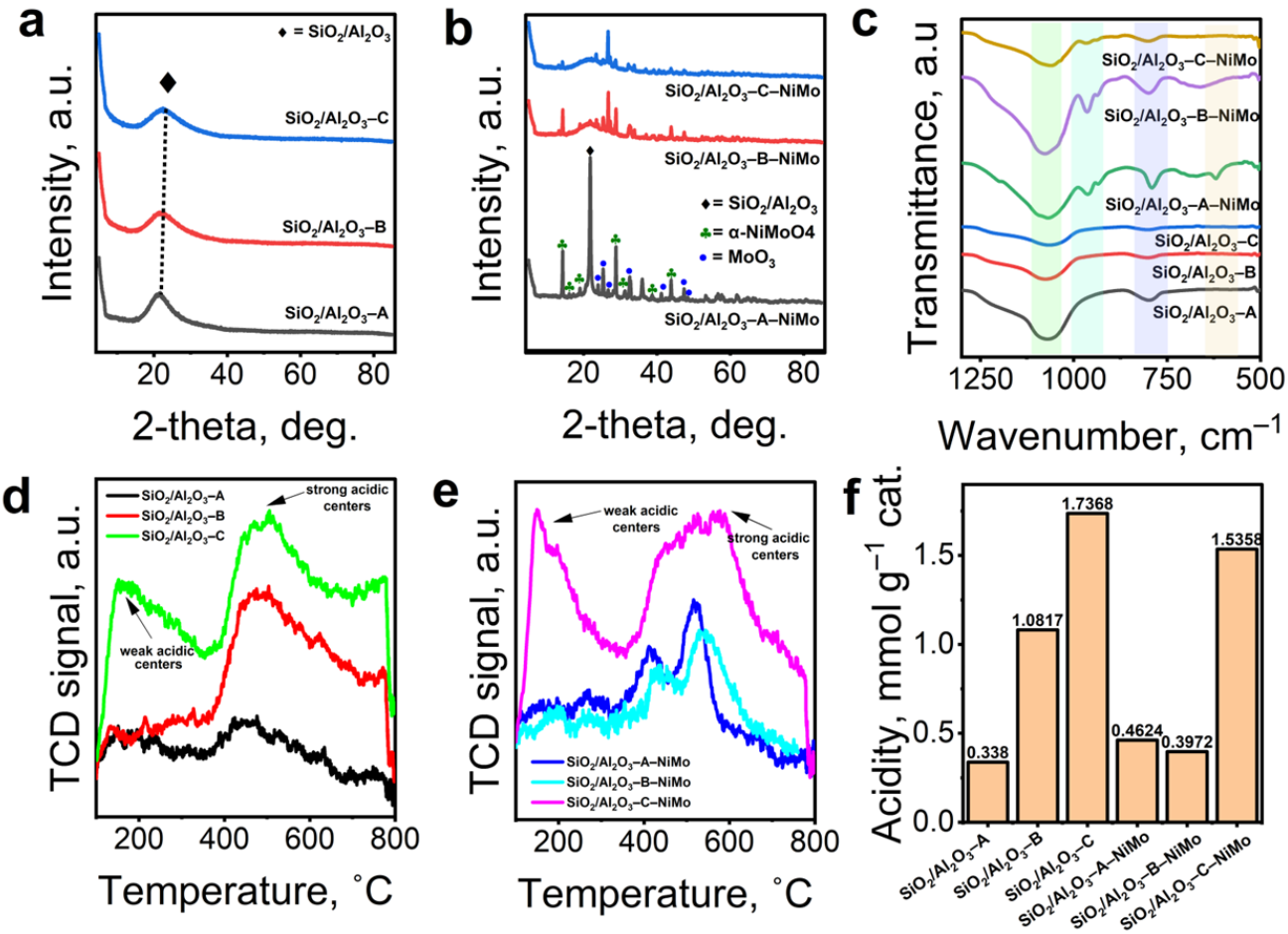

Figure 1. a) XRD pattern of SiO_2/Al_2O_3 b) XRD pattern of SiO_2/Al_2O_3–NiMo. SiO_2/Al_2O_3–x exhibits an amorphous structure, with the corresponding peak shifting toward higher 2θ values and decreasing in intensity. SiO_2/Al_2O_3–x–NiMo exhibits a crystalline structure with intensity decreasing upon elevating Al weight. c) IR spectra of SiO_2/Al_2O_3 and SiO_2/Al_2O_3–NiMo. The absorption bands of SiO_2/Al_2O_3–x shift to lower wavenumber, and the shoulder weakens upon elevating Al weight. New absorption bands in SiO_2/Al_2O_3–x–NiMo are observed arising from inherent NiMo bonding or interactions with the support. d) NH_3-TPD profile of SiO_2/Al_2O_3. Elevating Al weight in SiO_2/Al_2O_3 alters the acidic sites and forms strong acid center (~450 ˚C). SiO_2/Al_2O_3–x–NiMo displays varying acidity features depending on the Al weights.e) NH_3-TPD profile of SiO_2/Al_2O_3–NiMo f) Acidity of catalysts calculated from NH_3-TPD. SiO_2/Al_2O_3 was varying at different weights, where A = 5 g, B = 10 g, C = 25 g of Al.

[41]. Shoulder around 1093 cm^{-1} and 713 cm^{-1} can arise from Si–O/Al–O influenced by NiMo species [42]. The intensity of Ni–O/Mo–O bands decrease as aluminium weight increases, consistent with stronger metal–support interactions (Ni–O–Al, Mo–O–Al) and fewer "free" metal–oxygen groups. Compared with the parent supports, Si–O–Si stretching in SiO_2/Al_2O_3–A–NiMo shifts to higher wavenumber, indicating modification of the silanol environment by NiMo–support interaction, in agreement with reports on metal–modified silicas [43,44].

To understand the surface acidity of catalysts, including their corresponding acid density and strength, NH_3 temperature–programmed desorption (NH_3–TPD) analysis was performed as shown in Figure 1d-e. The desorption peaks of NH_3 at different temperatures correspond to different acidic centers strengths. For instance, desorption peaks at < 200 ˚C, 200 – 300 ˚C, and >300 ˚C are attributed to weak, medium, and strong acidic centers, respectively [45]. The corresponding acidity value (mmol.g-cat^{-1}) extracted from the NH_3–TPD profile are summarized in Figure 1f.

It is apparent that NH_3–TPD profiles of the parent SiO_2/Al_2O_3–A (Figure 1d) exhibit a desorption peak at ~450 ˚C indicating the presence of strong acidic sites. This peak may originate from bridging hydroxyl groups (Si–OH–Al) within the support [46]. Increasing aluminium weight to 10 g (SiO_2/Al_2O_3–A) resulted in a higher intensity of this desorption, suggesting an increase in the density of the acidic sites. The peak also slightly shifted to higher temperature, suggesting an increase in strong acidic strength as well [47]. A similar trend was observed for SiO_2/Al_2O_3–C (25 g aluminium weights), where the peak possessed much higher intensity in strong acidic sites and a further shift to higher temperature, indicating even stronger acidic sites. The acidity value of the SiO_2/Al_2O_3 catalysts followed the trend: SiO_2/Al_2O_3–A (0.3380 mmol.g-cat^{-1}) < SiO_2/Al_2O_3–B (1.0817 mmol.g-cat^{-1}) < SiO_2/Al_2O_3–C (1.7368 mmol.g-cat^{-1}) (Figure 1f). This trend suggests that increasing the aluminium weights in SiO_2/Al_2O_3 linearly enhances the strong acidic sites and density due to more aluminium species being available to induce acidic sites [33]. This trend is also consistently reported by another study, which proposed that the acid site density increases linearly as increasing aluminium content (or decreasing Si/Al ratio) [48]. Interestingly, a new desorption peak at ~150 ˚C appeared in SiO_2/Al_2O_3–C, suggesting that higher aluminium weights in the support promote the formation of low acidic sites. This may arise from extra-framework aluminium species [49].

The distribution of the acidic strength and density of the support catalysts considerably changed upon being loaded with NiMo (Figure 1e). For instance, SiO_2/Al_2O_3–A–NiMo exhibited new desorption peak at ~410 ˚C and ~515 ˚C, corresponding to strong acidic sites, and at ~265 ˚C, attributed to moderate acidic sites. These peaks may arise from the formation of new strong Lewis and Brønsted acid sites induced by NiMo species anchored on SiO_2/Al_2O_3. The moderate acidic sites may be attributed to Al–OH groups/silica frameworks interacting with NiMo species. Compared to the parent catalyst, the acidity value slightly increased to 0.4624 mmol.g-cat^{-1}. Additionally, the desorption peaks in SiO_2/Al_2O_3–A–NiMo were much broader with higher intensity compared to those of SiO_2/Al_2O_3–A catalyst, which was presumably due to better contact of NiMo species with the support [50]. Likewise, SiO_2/Al_2O_3–B–NiMo also exhibited new narrow desorption peak at ~530 ˚C and ~ 430 ˚C attributed to strong acidic sites but showing an opposite trend in term of desorption intensity compared to SiO_2/Al_2O_3–B. The decrease of peak desorption may arise from NiMo aggregation hindering the nature of SiO_2/Al_2O_3 acidic sites [51], and thus reducing the acidity value to 0.3972 mmol.g-cat^{-1}. Meanwhile, SiO_2/Al_2O_3–C–NiMo shows similar desorption peaks with SiO_2/Al_2O_3–C, but the strong acidic site desorption peak tended to shift to higher temperature, associated with a decrease in its intensity. The shift of the desorption peak to higher temperature may indicate stronger interaction between the metal and the support. The low acidic sites in SiO_2/Al_2O_3–C–NiMo possess much higher intensity than its parent catalyst. This may be ascribed to the weak Lewis acid sites of metal species that are well dispersed [51]. However, pore blocking may cover the acidic sites, thus decreasing the acidity value to 1.5358 mmol.g-cat^{-1} compared to its parent SiO_2/Al_2O_3–C catalyst. The acidity features from NH_3-TPD profiles of SiO_2/Al_2O_3–x–NiMo prepared with KHP are found to be different compared to the previous study employing EDTA as a template agent [33], confirming that use of different template agent influence the acidity strength and distribution. It is also noticeable that the acidity value of the catalysts prepared with KHP are higher compared to those prepared with EDTA. This may happen due to strong coordination with M^{n+} from the support of loaded metal which may reduce the strong acidic sites upon calcination. Whereas KHP, it is an aromatic organic acid that decomposes differently compared to EDTA, which may result in a higher density of M–OH groups that enhance the acidity value.

Nitrogen adsorption–desorption and BJH desorption representing the textural features of catalysts are shown in Figure 2. As shown in Figure 2a-c, the parent SiO_2/Al_2O_3 and SiO_2/Al_2O_3–NiMo catalysts possess type IV isotherm indicate mesoporous materials [52]. Upon varying the aluminium weight, however, the catalysts exhibit different hysteresis types, suggesting different pore structures such as its connectivity or the degree of pore filling. The BJH desorption associating the pore size distribution of catalysts is presented in Figure S1 (Supporting Information). Broad pore size distribution with a wide range of pore sizes was observed in SiO_2/Al_2O_3–A. This may arise from the heterogeneity in pore structure. The intensity of this peak is much lower than its counterparts, as it exhibits low surface area and total pore volume (Table 1). Upon increasing the aluminium weight to 10 g (SiO_2/Al_2O_3–B), a narrow pore size distribution in the small mesoporous ranges was observed. This may indicate that increasing the aluminium weight promotes better pore uniformity and a more defined pore size distribution. Meanwhile, SiO_2/Al_2O_3–C shows a similar trend to SiO_2/Al_2O_3–B in its peak maxima but with much wider pore size distribution, which suggests the formation of predominant diverse pore network. It may therefore be proposed that increasing the aluminium weight in SiO_2/Al_2O_3 enhances the mesoporosity development of the catalyst. This interpretation is consistent with earlier reports [33], where increasing aluminium content led to a substantial rise in BET surface area and total pore volume, while the average pore diameter remained in the mesoporous regime. Such concurrent trends, with stable mesopore size, are considered as characteristic of improved mesoporosity. Similarly, studies on Al-SBA-15 have shown that higher aluminium incorporation decreases blocked pores, increases mesopore volume due to aluminium species interacting with silanol groups and reinforcing the framework, thereby promoting the formation of primary mesopores [53].

The peak maxima in SiO_2/Al_2O_3–A-NiMo and SiO_2/Al_2O_3–B–NiMo (Figure S1b-c) disappeared upon being loaded with NiMo, indicating that the NiMo species may have modified or blocked the pores in the smaller pore size range. This may

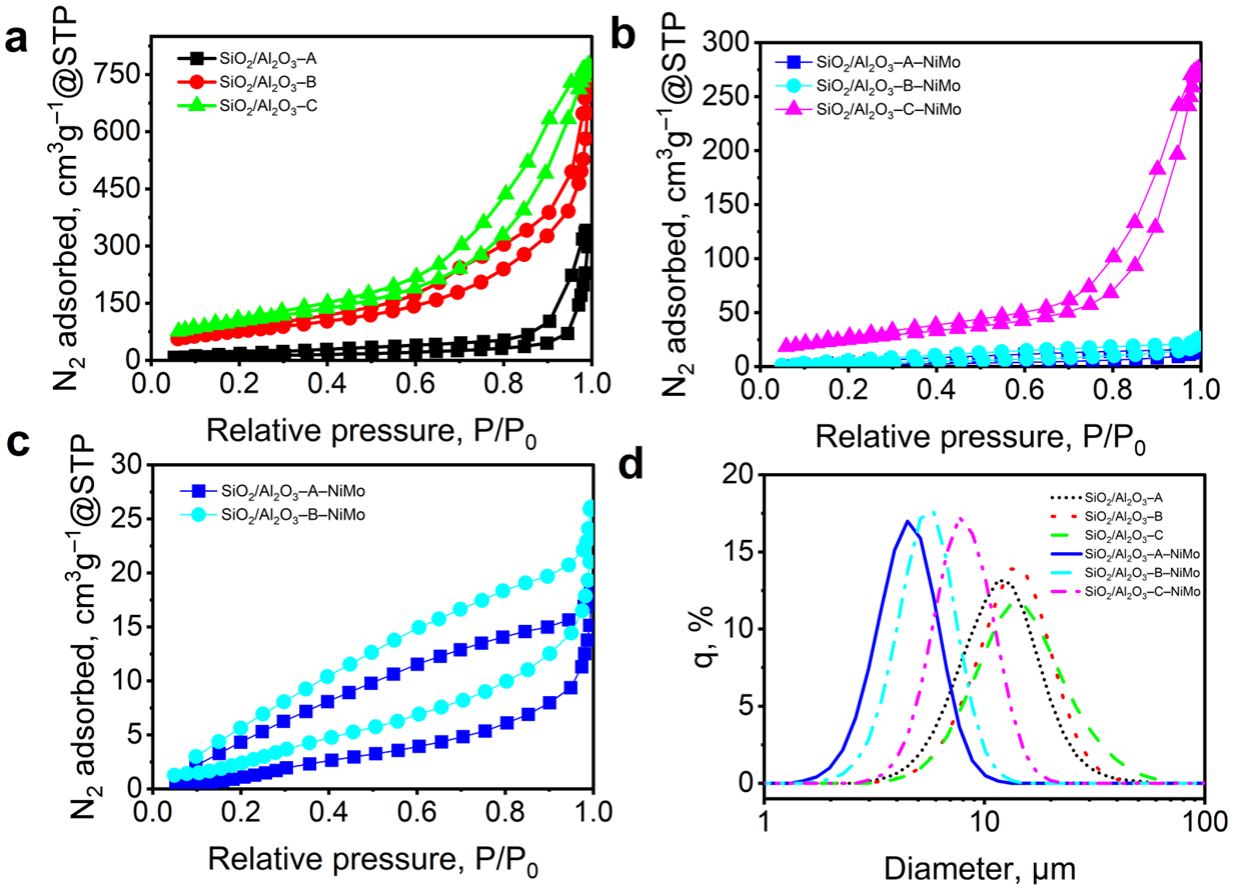

Figure 2. a) N_2 physisorption of SiO_2/Al_2O_3; b) a) N_2 physisorption of SiO_2/Al_2O_3–NiMo; c) enlargement of SiO_2/Al_2O_3–NiMo-A, and -B. All catalysts exhibit type IV isotherm with different hysteresis types. BJH desorption shows varying pore size distribution depending on Al weights; d) Particle size distribution extracted from particle size analyzer in μm scale of SiO_2/Al_2O_3 and SiO_2/Al_2O_3–NiMo at varying aluminium weights. SiO_2/Al_2O_3–x–NiMo exhibits a narrower particle size distribution, higher quantile percentages, and a shift to smaller diameter compared to SiO_2/Al_2O_3–x.

happen due to the NiMo species filling up the mesopores. For SiO_2/Al_2O_3–C–NiMo, the maxima peak was still present but with a much wider pore size distribution along with the decrease in its intensity. This may suggest that the NiMo species altered the mesopore size distribution, resulting in larger pores formation. The decrease in intensity may be attributed to the partial blocking or filling the mesopores, but to a lesser degree than SiO_2/Al_2O_3–A-NiMo and SiO_2/Al_2O_3–B–NiMo. The BET surface area, total pore volume, and average pore diameter are summarized in Table 1. Based on Table 1, SiO_2/Al_2O_3–A exhibits surface area of 40.75 $m^2.g^{-1}$. The surface area tended to increase up to 281.20 $m^2.g^{-1}$ upon elevating aluminium weight to 10 g (SiO_2/Al_2O_3–A) due to pore expansion arising from Si–O–Al bonding or formation a new pore induced by Al atoms. Similarly, elevating aluminium weight to 25 g (SiO_2/Al_2O_3–C) linearly increased the surface area to 373.60 $m^2.g^{-1}$. This indicates that increasing aluminium weight in SiO_2/Al_2O_3 would enhance the textural features of catalyst by increasing porosity. Upon being loaded with NiMo, the surface area of parent catalyst tended to dramatically decrease to 8.76 $m^2.g^{-1}$ (SiO_2/Al_2O_3–A–NiMo). Similarly, SiO_2/Al_2O_3–B–NiMo and SiO_2/Al_2O_3–C–NiMo exhibited a decrease in surface area to 13. 15 $m^2.g^{-1}$ and 92.08 $m^2.g^{-1}$, respectively, compared to their parent catalyst. This may point out the pore blockage by NiMo species [54]. This result is consistent with the XRD analysis, as higher aluminium weight in parent SiO_2/Al_2O_3 catalyst corresponds to amorphous structure and it contributes to higher surface area with more interconnected pores. The XRD analysis of SiO_2/Al_2O_3–NiMo also reveals the potential of aggregated crystalline NiMo phase, in which assuming if the NiMo are poorly dispersed, it may block the pores. Table 1 also shows that the parent SiO_2/Al_2O_3 catalysts exhibit an increase in total pore volume upon elevating aluminium weight. This points out that higher aluminium weights are associated with higher pore volume. Upon being loaded with NiMo, the total pore volume of catalyst at all varying aluminium weights tended to decrease which again, it arises due to pore blockage of the SiO_2/Al_2O_3 by NiMo particles [55]. It assumes that the low total pore volumes in SiO_2/Al_2O_3–NiMo catalysts indicate that the NiMo species occupied or covered a fraction of the pore. In terms of average pore diameter, the pore diameter of parent catalysts increased upon elevating aluminium weight. Although catalytic activity is not only affected by textural features, however, larger pore volume coupled with higher BET surface area may reduce the mass transfer resistance and better metal dispersion which beneficial to the catalytic reaction [56].

The average pore diameter of catalysts showed different trends upon being loaded with NiMo. For instance, SiO_2/Al_2O_3–A–NiMo and SiO_2/Al_2O_3–B–NiMo exhibited a decrease in average pore diameter to 13.46 nm and 11.85 nm, respectively with respect to their parent catalyst due to metal deposition inside the pores [57]. For SiO_2/Al_2O_3–C–NiMo, however, the average pore diameter increased to 18.48 nm which may arise from the deposition on the surface or wider pores rather than occupies internal pores. Based on textural analysis, it is proposed that higher aluminium weight promotes enhanced metal–support interaction (M–O–Al bonds, where M = Ni or Mo), increasing uniform dispersion. The blockage of pores without severe agglomeration may arise from this interaction, as confirmed by XRD, FTIR, and NH_3–TPD analysis. It is noteworthy that the parent catalysts SiO_2/Al_2O_3 and upon being loaded with NiMo prepared with KHP had much higher value in terms of surface area, total pore volume, and average pore diameter compared to the previous study utilizing EDTA as a template agent [33]. This confirms that the choice of templating agent influences the textural features of SiO_2/Al_2O_3. Similar observations have been reported in related studies, where catalysts synthesized with KHP as a template consistently showed higher surface area than those prepared with EDTA [25]. These differences have been attributed to the distinct role of organic templates during gel formation and

Table 1. Textural properties of SiO_2/Al_2O_3 supports and SiO_2/Al_2O_3–NiMo catalysts with varying aluminium weights.

Catalyst	BET surface area, $m^2.g^{-1}$	Total pore volume, $cm^3.g^{-1}$	Average pore diameter, nm
SiO_2/Al_2O_3–A	40.75	0.52	51.24
SiO_2/Al_2O_3–B	281.20	1.11	15.82
SiO_2/Al_2O_3–C	373.60	1.20	12.83
SiO_2/Al_2O_3–A–NiMo	8.76	0.03	13.46
SiO_2/Al_2O_3–B–NiMo	13.50	0.04	11.85
SiO_2/Al_2O_3–C–NiMo	92.08	0.43	18.48

decomposition, which govern pore development [58].

Figure 2d presents the particle size distribution in µm scale of SiO_2/Al_2O_3 and SiO_2/Al_2O_3–NiMo at varying aluminium weights. The average particle size (µm) from the particle size analyzer is summarized in Table S1 (Supporting Information). As shown in Figure 2d, parent SiO_2/Al_2O_3–A exhibited a relatively narrow particle size distribution and peak slightly shift to higher diameter as aluminium weight increased. This indicates that varying aluminium weight may influence the growth or aggregation of SiO_2/Al_2O_3 particles, consistent with reports that Si/Al composition strongly affects particle assembly and aggregation during synthesis [59]. However, in terms of its intensity, it exhibited nonlinear trends. For instance, the intensity tended to increase as elevating aluminium weight increases at intermediate aluminium weight, suggesting more uniform particle formation. The intensity subsequently decreased at higher aluminium weight (SiO_2/Al_2O_3–C) owing to the partial aggregation of particle or less uniformity. Similar effects have been reported in oxide-based catalyst systems, where compositional or metal incorporation influenced particle aggregation behavior [34,39].

Upon being loaded with NiMo, the particle size distribution became narrower and shifted to lower diameter, which presumably suggests that NiMo particles occupied surface/pore voids along with more uniform particles. The intensity also increased upon being loaded with NiMo, which may be attributed to better interaction between NiMo and the support catalyst. Table S1 (Supporting Information) shows that the average particle size of parent catalysts linearly increases as elevating aluminium weight due to potential stronger interaction between particles and thus potentially form aggregates. Furthermore, the average particle size decreased upon being loaded with NiMo. This result may strengthen the notion that NiMo particles are evenly distributed, presumably filling pore voids. Based on the Table S1, within the SiO_2/Al_2O_3–NiMo catalyst, SiO_2/Al_2O_3–C–NiMo shows much higher in average particle size than its counterparts (SiO_2/Al_2O_3–A–NiMo and SiO_2/Al_2O_3–B–NiMo), which may indicate higher degree interaction of NiMo between the support. This result is consistent with the FTIR and XRD analysis as previously discussed.

The surface morphology of SiO_2/Al_2O_3 support and SiO_2/Al_2O_3–NiMo at varying aluminium weights was analyzed using scanning electron microscopy (SEM). As shown in Figure 3, the SEM micrographs of SiO_2/Al_2O_3 show irregular shapes of aggregate particles, and these features are much pronounced as increasing the aluminium weight, which may suggest higher degree aggregation due to the formation of SiO_2/Al_2O_3 support. The morphology also shows a smooth surface associated with its amorphous structure. Upon being loaded with NiMo, a pronounced change in the morphological surface of support is observed. It is apparent that the pore connectivity was more developed and NiMo particles were

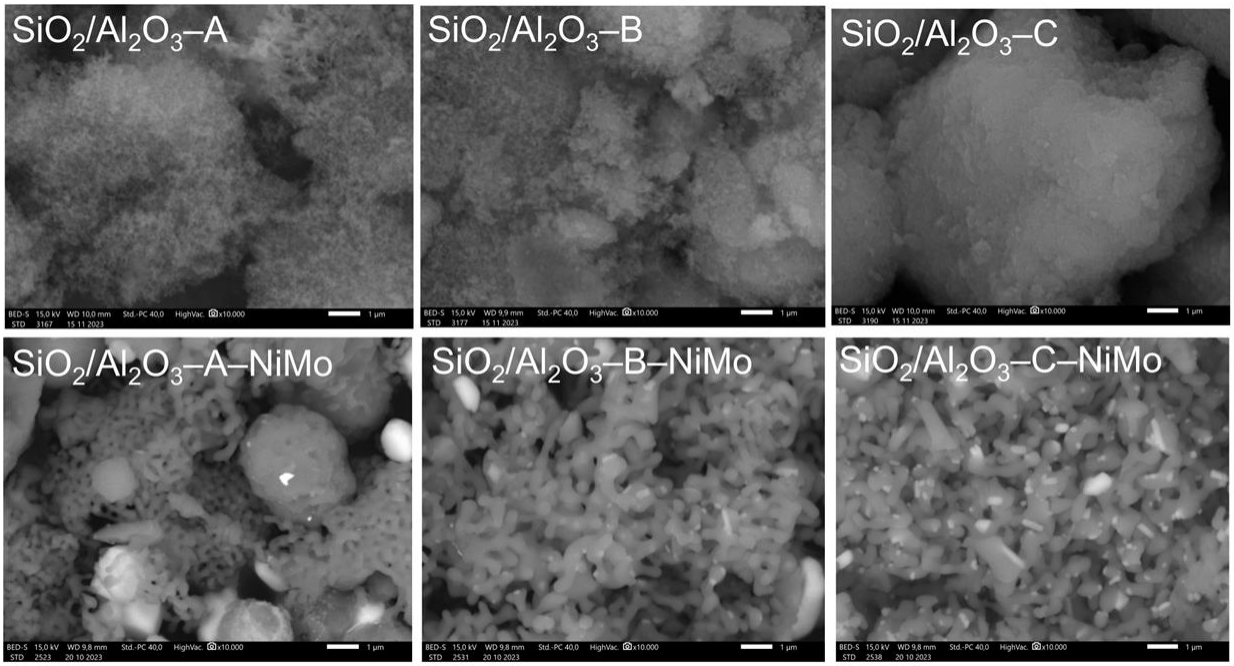

Figure 3. SEM micrographs of SiO_2/Al_2O_3 support and SiO_2/Al_2O_3–NiMo at varying aluminium weights (10000× magnification). All catalysts were utilized KHP as template agents. SiO_2/Al_2O_3–x–NiMo shows more pronounce porous features compared to SiO_2/Al_2O_3–x depending on the Al weights.

better distributed at higher aluminium weights due to the NiMo interaction with the support.

Figure 4 shows the EDS-mapping of the catalysts. It is noteworthy that in SiO_2/Al_2O_3–A–NiMo the NiMo particles exhibit poor dispersion due to aggregation within the support catalyst. Similar results were also observed in SiO_2/Al_2O_3–B–NiMo. However, in SiO_2/Al_2O_3–C–NiMo, the NiMo particles are well dispersed and evenly distributed within the support catalyst. This result confirms that increasing the aluminium weights in the support enhances the metal dispersion of NiMo. This analysis is consistent with the structural and textural analysis.

3.2 Catalytic Activity

The hydrocracking of CPO was performed at 350 ˚C for 2 h under hydrogen pressure of 20 bar. Figure 5 and Figure S2 (Supporting Information) summarize the catalytic performance of SiO_2/Al_2O_3 and SiO_2/Al_2O_3–NiMo at varying aluminium weights. The overall CPO conversion (Figure S2) ranges from ~86 to 95%, though the extent of distribution of products varies systematically with aluminium weights and NiMo loading (Figure 5). For the parent catalysts, increasing the aluminium weights (SiO_2/Al_2O_3–A and SiO_2/Al_2O_3–B) enhanced both conversion (85.85 to 91.81 %) and the product distribution, which shifted from oxygenate-rich, C_{10}-C_{14} dominated fractions toward jet-range hydrocarbon and aromatics (Figure 5). This trend is consistent with the XRD, FTIR, and NH_3–TPD results, which confirm that higher aluminium weights enhance acidity, strengthens Si–O–Al interactions, and promotes mesoporosity

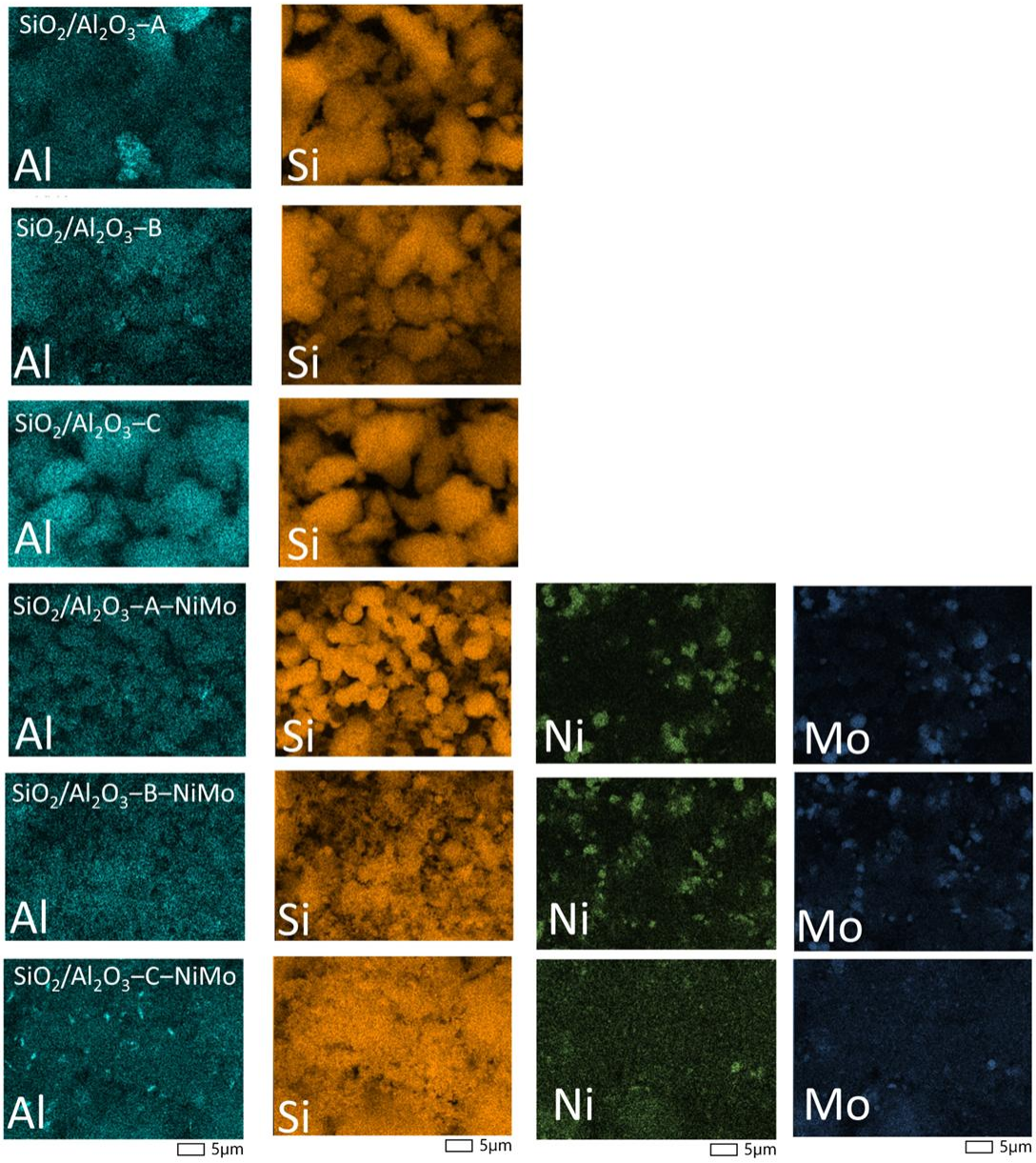

Figure 4. EDS mapping of SiO_2/Al_2O_3 support and SiO_2/Al_2O_3–NiMo at varying Al weights. Different colors represent different types of elements. Higher Al weights enhance NiMo dispersion (orange and dark blue colors, respectively) in SiO_2/Al_2O_3–NiMo.

structure, thus providing the β-scission forming C_5-C_{14} fractions (gasoline/jet range), skeletal isomerization forming branched iso-paraffins, and dehydrogenation/cyclization of long-chain carbons [60]. Upon NiMo loading, the catalysts exhibit a metal function that accelerates deoxygenation pathway [61]. Ni and Mo species hydrogenate C=O as well as C=C bonds and thus catalyze hydrodeoxygenation (HDO) (R–COOH → n-alkane + H_2O) as well as decarboxylation/decarbonylation (deCOx) (R–COOH → n-alkane + CO/CO_2). As a result, SiO_2/Al_2O_3–NiMo exhibited a sharp reduction in oxygenates and the emergence of n-alkanes in the C_{15}-C_{18} range, which are subsequently cracked and isomerized on acid sites to afford jet-range iso-paraffins and aromatics (Figure 5). This metal–acid synergy explains the higher conversions observed in SiO_2/Al_2O_3–A–NiMo (95.02 %) and SiO_2/Al_2O_3–B–NiMo (94.20 %) relative to their parent catalysts. It is noteworthy that SiO_2/Al_2O_3–C–NiMo showed a lower conversion (88.97 %) compared to its parent (91.81 %) (Figure S5), which may be attributed to partial blockage and decreased surface area upon NiMo loading, as revealed by BET and BJH analyses. Although its acidity and dispersion remain high, the reduced accessibility of acid sites likely limited, even as the product distribution of jet-range and aromatic hydrocarbons remained high. Table 2 summarizes the previous study on palm oil hydrocracking using different catalysts and templating approaches. The catalytic performance of the present KHP–templated SiO_2/Al_2O_3–NiMo is comparable with, and in several cases superior to, other reported systems for CPO hydrocracking. While various catalysts have achieved good overall conversion, the as-prepared catalyst stands out by combining high conversion with good product distribution toward jet fuel range hydrocarbon.

It is proposed that these results support a mechanistic picture in which NiMo sites act as the primary deoxygenation centers, producing long-chain n-alkanes from fatty acid, while SiO_2/Al_2O_3 promote subsequent cracking, isomerization, and aromatization as summarized in Figure 6. The interplay between acidity, porosity, and metal dispersion dictates both conversion and product distribution. For instance, low aluminium weight catalysts lack sufficient acidity to drive the reactions, high aluminium weight catalysts risk

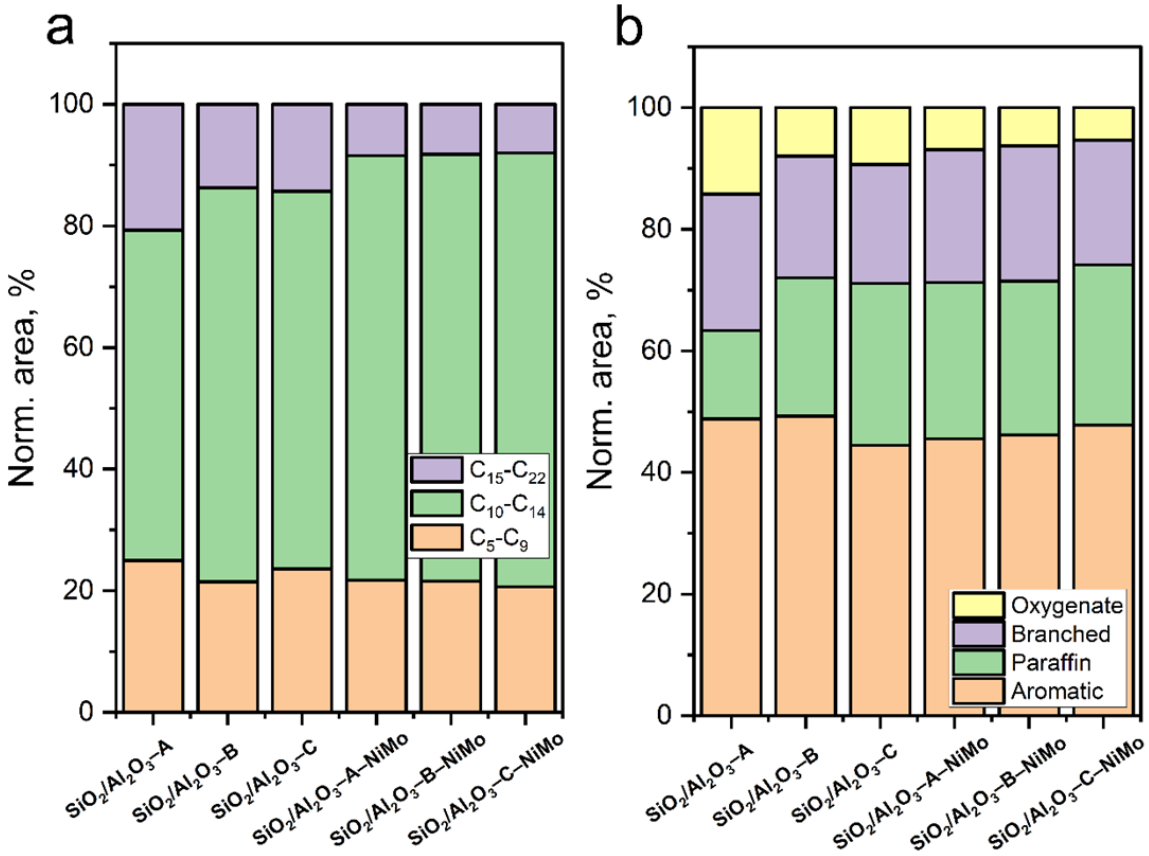

Figure 5. Normalized product distribution from GC-MS analysis of hydrocracking products over SiO_2/Al_2O_3 and SiO_2/Al_2O_3–NiMo catalysts with varying aluminium weights. a) carbon-number distribution, classified into gasoline (C_5-C_9), jet fuel (C_{10}-C_{14}), and diesel (C_{15}-C_{22}) fractions. b) Chemical compositions of products categorized as aromatic hydrocarbon, paraffins, branched iso-paraffins, and residual oxygenated species. Product areas were normalized to 100% for each catalyst to enable comparison of relative selectivity.

Table 2. Comparison of catalytic activity of different catalysts reported for palm oil hydrocracking. The table summarizes reaction conditions, conversion, and products distribution are listed as reported in the original studies.

Catalyst	Reaction conditions	Catalytic activity	Ref.
NiW-ZSM-5 (Si/Al = 50)	T = 400 ˚C for 2 h; P H_2= 3-8 MPa; feed = 500 mL CPO; cat. = 5 g; stir = 500 rpm.	Conversion = 96 wt%, kerosene yield = 22.36 wt%, gasoline yield = 12.44 wt%, diesel yield = 21.22%.	[15]
ZSM- 5/MCM-41	T = 400 ˚C for 2 h; feed = 500 mL CPO; cat. 5 g; P H_2 = 3 mPa; stir = 500 rpm	Conversion = 51.00 %, kerosene yield = 20.60 %, gasoline yield = 9.23 %, diesel yield = 21.17 %.	[62]
Al_2O_3/ Pd-Fe (PF3)	T = 400 ˚C for 2 h; feed = 100 mL; cat. 0.9 g; P H_2 = 60 bar.	Kerosene yield = 31.71 %, diesel yield = 62.20 %.	[10]
SiO_2/ZrN-EDTA	T = 500 ˚C for 1 h; feed flow rate = 20 mL/h, H_2 flow rate = 30 mL/h, cat. = 0.5 g.	Conversion = 94.36 %, gasoline selectivity = 30.74 %, kerosene selectivity = 63.79 %, diesel selectivity = 5.47 %	[25]
SiO_2/ZrN-KHF	T = 500 ˚C for 1 h; feed flow rate = 20 mL/h, H_2 flow rate = 30 mL/h, cat. = 0.5 g.	Conversion = 96.02 %, gasoline selectivity = 71.05 %, kerosene selectivity = 24.88 %, diesel selectivity = 4.07 %	[25]
SiO_2/Zr-KHF2	T = 500 ˚C for 1 h; feed flow rate = 20 mL/h, H_2 flow rate = 30 mL/h, cat. = 0.5 g.	Conversion = 95.53 %, gasoline selectivity = 24.72%, jet selectivity = 69.27%, diesel selectivity = 6.01%.	[17]
SiO_2-Al_2O_3-10/NiMo (EDTA template)	T = 350 ˚C for 2 h; feed = 20 g CPO; P H_2 20 bar; stir = 1500 rpm.	Conversion = 91.34 %, gasoline yield = 13.26 %, jet yield = 61.31 %, diesel yield = 2.34 %.	[33]
SiO_2-Al_2O_3-10/NiMo (KHP template)	T = 350 ˚C for 2 h; feed = 20 g CPO; P H_2 20 bar; stir = 1500 rpm.	Conversion = 94.2 %, gasoline fraction = 21.59 %, jet fraction = 70.21 %, diesel fraction = 8.2 %.	This study

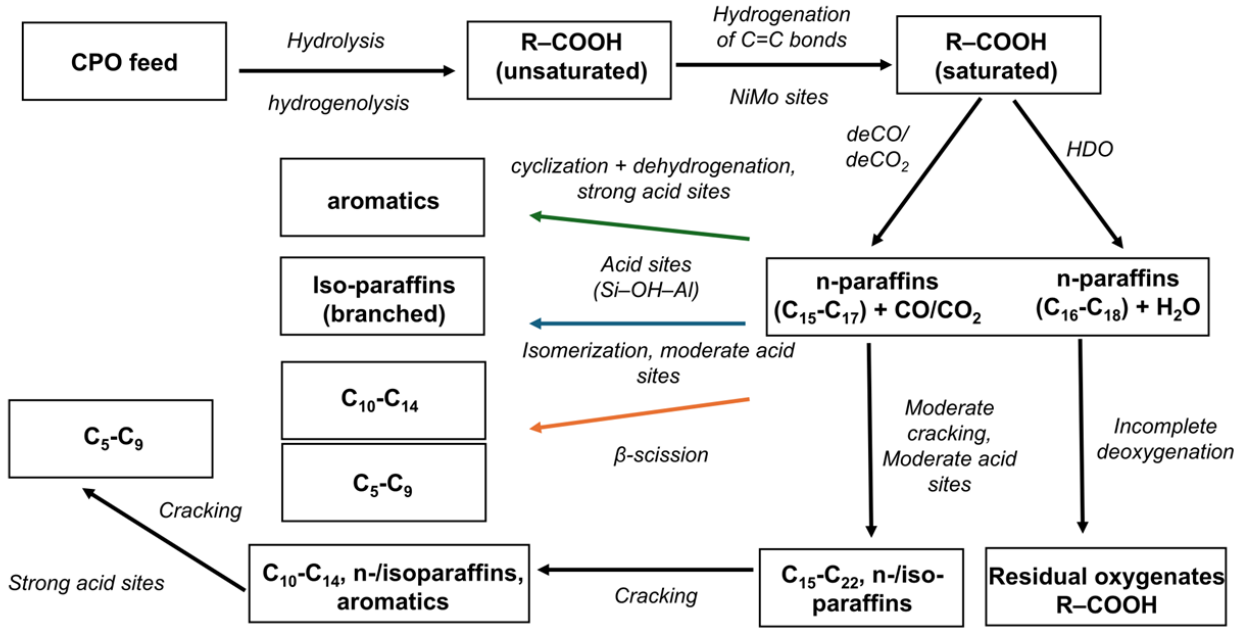

Figure 6. Proposed mechanistic pathway for hydrocracking of CPO over SiO_2/Al_2O_3–NiMo catalysts.

textural constraints upon NiMo loading, and intermediate aluminium weight provides the most balanced environment. This is exemplified by SiO_2/Al_2O_3–B–NiMo, which afforded high conversion alongside efficient oxygen removal and favorable product distribution toward jet-range hydrocarbon and aromatics.

4. Conclusions

This study highlights the significance of potassium hydrogen phthalate (KHP) as a templating agent for SiO_2/Al_2O_3–NiMo catalysts in crude palm oil hydrocracking. Compared with EDTA-templated analogues, KHP–templated catalysts exhibit higher surface area, larger pore volume, and stronger acidity, enabling better NiMo dispersion and improved product distribution toward jet fuel-range hydrocarbons. Within the KHP–templated series, aluminium weight acts as a tunable handle that governs Si–O–Al formation, acidity distribution, mesoporosity, and metal dispersion; an intermediate aluminium weight provides the best balance of accessible acid sites and NiMo exposure, whilst excessive aluminium increases acidity but can reduce accessibility after metal loading. These outcomes underscore that both template choice and aluminium weight jointly control structure–acidity–dispersion relationships in SiO_2/Al_2O_3–NiMo, providing practical guidance for designing mesoporous bifunctional catalysts for biofuel production.

Acknowledgment

The authors gratefully acknowledge DRPM Ministry of Education, Culture, Research and Technology, Indonesia, for funding this research through Penelitian Fundamental research grant SPPK no. 050/E5/PG.02.00.PL/2024.

CRedit Author Statement

Author Contributions: Hasanudin Hasanudin: Conceptualization, Methodology, Supervision, Writing - Review & Editing, Funding acquisition. Mhika Nakashima: Investigation, Writing - original draft preparation. Wan Ryan Asri: Writing - original draft preparation, Data curation. Roni Maryana: Resource, Supervision. Muhammad Al Muttaqii: Resource, Formal analysis. Nino Rinaldi: Resource, Formal analysis. Fitri Hadiah: Resource, Formal analysis. Novia Novia: Resource, Formal analysis. All authors have read and agreed to the published version of the manuscript.

References

[1] Wei, Q., Zhang, P., Liu, X., Huang, W., Fan, X., Yan, Y., Zhang, R., Wang, L., Zhou, Y. (2020). Synthesis of Ni-Modified ZSM-5 Zeolites and Their Catalytic Performance in n-Octane Hydroconversion. *Frontiers in Chemistry*, 8 (December), 1–8. DOI: 10.3389/fchem.2020.586445.

[2] Wang, J., Singer, S.D., Souto, B.A., Asomaning, J., Ullah, A., Bressler, D.C., Chen, G. (2022). Current progress in lipid-based biofuels: Feedstocks and production technologies. *Bioresource Technology*, 351(March), 127020. DOI: 10.1016/j.biortech.2022.127020.

[3] Mancio, A.A., da Costa, K.M.B., Ferreira, C.C., Santos, M.C., Lhamas, D.E.L., da Mota, S.A.P., Leão, R.A.C., de Souza, R.O.M.A., Araújo, M.E., Borges, L.E.P., Machado, N.T. (2016). Thermal catalytic cracking of crude palm oil at pilot scale: Effect of the percentage of Na2CO3 on the quality of biofuels. *Industrial Crops and Products*, 91, 32–43. DOI: 10.1016/j.indcrop.2016.06.033.

[4] Alisha, G.D., Trisunaryanti, W., Syoufian, A., Larasati, S. (2023). Synthesis of high stability Mo/SiO2 catalyst utilizing Parangtritis beach sand for hydrocracking waste palm oil into biofuel. *Biomass Conversion and Biorefinery*, 13, 11041–11055. DOI: 10.1007/s13399-021-02064-x.

[5] Allwar, A., Maulina, R., Julianto, T.S., Widyaningtyas, A.A. (2022). Hydrocracking of crude palm oil over bimetallic oxide Nio-CdO/biochar catalyst. *Bulletin of Chemical Reaction Engineering & Catalysis*, 17(2), 476–485. DOI: 10.9767/bcrec.17.2.14074.476-485.

[6] Liu, Y., Murata, K., Inaba, M. (2019). Hydrocracking of algae oil to aviation fuel-ranged hydrocarbons over NiMo-supported catalysts. *Catalysis Today*, 332, 115–121. DOI: 10.1016/j.cattod.2018.07.047.

[7] Anand, M., Farooqui, S.A., Kumar, R., Joshi, R., Kumar, R., Sibi, M.G., Singh, H., Sinha, A.K. (2016). Optimizing renewable oil hydrocracking conditions for aviation bio-kerosene production. *Fuel Processing Technology*, 151, 50–58. DOI: 10.1016/j.fuproc.2016.05.028.

[8] Sihombing, J.L., Pulungan, A.N., Herlinawati, H., Yusuf, M., Gea, S., Agusnar, H., Wirjosentono, B., Hutapea, Y.A. (2020). Characteristic and catalytic performance of Co and Co-Mo metal impregnated in sarulla natural zeolite catalyst for hydrocracking of MEFA rubber seed oil into biogasoline fraction. *Catalysts*, 10(1), 1–14. DOI: 10.3390/catal10010121.

[9] Dujjanutat, P., Kaewkannetra, P. (2020). Production of bio-hydrogenated kerosene by catalytic hydrocracking from refined bleached deodorised palm/palm kernel oils. *Renewable Energy*, 147, 464–472. DOI: 10.1016/j.renene.2019.09.015.

[10] Srihanun, N., Dujjanutat, P., Muanruksa, P., Kaewekannetra, P. (2020). Biofuels of green diesel– kerosene–gasoline production from palm oil : Effect of palladium cooperated with second metal on hydrocracking reaction. *Catalysts*, 10(2), 241. DOI: 10.3390/catal10020241.

[11] Lanzafame, P., Perathoner, S., Centi, G., Heracleous, E., Iliopoulou, E.F., Triantafyllidis, K.S., Lappas, A.A. (2017). Effect of the Structure and Mesoporosity in Ni/Zeolite Catalysts for n-Hexadecane Hydroisomerisation and Hydrocracking. *ChemCatChem*, 9(9), 1632–1640. DOI: 10.1002/cctc.201601670.

[12] Escalona, G., Rai, A., Betancourt, P., Sinha, A.K. (2018). Selective poly-aromatics saturation and ring opening during hydroprocessing of light cycle oil over sulfided Ni-Mo/SiO2-Al2O3 catalyst. *Fuel*, 219(January), 270–278. DOI: 10.1016/j.fuel.2018.01.134.

[13] Papageridis, K.N., Charisiou, N.D., Douvartzides, S.L., Sebastian, V., Hinder, S.J., Baker, M.A., AlKhoori, S., Polychronopoulou, K., Goula, M.A. (2020). Effect of operating parameters on the selective catalytic deoxygenation of palm oil to produce renewable diesel over Ni supported on Al2O3, ZrO2 and SiO2 catalysts. *Fuel Processing Technology*, 209(July). DOI: 10.1016/j.fuproc.2020.106547.

[14] Saab, R., Polychronopoulou, K., Anjum, D.H., Charisiou, N.D., Goula, M.A., Hinder, S.J., Baker, M.A., Schiffer, A. (2022). Effect of SiO2/Al2O3 ratio in Ni/Zeolite-Y and Ni-W/Zeolite-Y catalysts on hydrocracking of heptane. *Molecular Catalysis*, 528(April), 112484. DOI: 10.1016/j.mcat.2022.112484.

[15] Subsadsana, M., Sangdara, P., Ruangviriyachai, C. (2017). Effect of bimetallic NiW modified crystalline ZSM-5 zeolite on catalytic conversion of crude palm oil and identification of biofuel products. *Asia-Pacific Journal of Chemical Engineering*, 12(1), 147–158. DOI: 10.1002/apj.2061.

[16] Kaewchada, A., Akkarawatkhoosith, N., Bunpim, D., Bangjang, T., Ngamcharussrivichai, C., Jaree, A. (2021). Production of bio-hydrogenated diesel from palm oil using Rh/HZSM-5 in a continuous mini fixed-bed reactor. *Chemical Engineering and Processing - Process Intensification*, 168(May), 108586. DOI: 10.1016/j.cep.2021.108586.

[17] Hasanudin, H., Asri, W.R., Mara, A., Muttaqii, M. Al, Maryana, R., Rinaldi, N., Sagadevan, S., Zhang, Q., Fanani, Z., Hadiah, F. (2023). Enhancement of catalytic activity on crude palm oil hydrocracking over SiO2/Zr assisted with potassium hydrogen phthalate. *ACS Omega*, 8(23), 20858–20868. DOI: 10.1021/acsomega.3c01569.

[18] Leyva, C., Ancheyta, J., Travert, A., Maugé, F., Mariey, L., Ramírez, J., Rana, M.S. (2012). Activity and surface properties of NiMo/SiO 2-Al 2O 3 catalysts for hydroprocessing of heavy oils. *Applied Catalysis A: General*, 425–426, 1–12. DOI: 10.1016/j.apcata.2012.02.033.

[19] Villarreal, A., Ramírez, J., Caero, L.C., Villalón, P.C., Gutiérrez-Alejandre, A. (2015). Importance of the sulfidation step in the preparation of highly active NiMo/SiO2/Al2O3 hydrodesulfurization catalysts. *Catalysis Today*, 250, 60–65. DOI: 10.1016/j.cattod.2014.03.035.

[20] Leyva, C., Ancheyta, J., Mariey, L., Travert, A., Maugé, F. (2014). Characterization study of NiMo/SiO2-Al2O3 spent hydroprocessing catalysts for heavy oils. *Catalysis Today*, 220–222, 89–96. DOI: 10.1016/j.cattod.2013.10.007.

[21] Prokić-Vidojević, D., Glišić, S.B., Krstić, J.B., Orlović, A.M. (2021). Aerogel Re/Pd-TiO2/SiO2 and Co/Mo-Al2O3/SiO2 catalysts for hydrodesulphurisation of dibenzothiophene and 4,6-dimethyldibenzothiophene. *Catalysis Today*, 378(July 2020), 10–23. DOI: 10.1016/j.cattod.2020.11.022.

[22] Li, M., Ihli, J., Verheijen, M.A., Holler, M., Guizar-Sicairos, M., Van Bokhoven, J.A., Hensen, E.J.M., Weber, T. (2022). Alumina-Supported NiMo Hydrotreating Catalysts─Aspects of 3D Structure, Synthesis, and Activity. *Journal of Physical Chemistry C*, 126(43), 18536–18549. DOI: 10.1021/acs.jpcc.2c05927.

[23] Yusefabada, E.T., Tavasoli, A., Zamani, Y. (2020). The performance of NiMo/SiO2-Al2O3 and NiMo/SO4-Al2O3 catalysts for hydrocracking of n-hexadecane. *Iranian Journal of Catalysis*, 9(2), 127–134.

[24] Hao, F., Zhong, J., Liu, P. Le, You, K.Y., Luo, H.A. (2012). Amorphous SiO2-Al2O3 supported Co3O4 and its catalytic properties in cyclohexane nitrosation to ε-caprolactam: Influences of preparation conditions. *Journal of Molecular Catalysis A: Chemical*, 363–364, 41–48. DOI: 10.1016/j.molcata.2012.05.014.

[25] Asri, W.R., Hasanudin, H., Wijaya, K. (2024). Hydroconversion of Crude Palm Oil Over Highly Dispersed Porous Silica Modified Zirconium Nitride: Effect of EDTA and KHF Template. *Silicon*, 16, 83–97. DOI: 10.1007/s12633-023-02659-1.

[26] Amaya, J., Suarez, N., Moreno, A., Moreno, S., Molina, R. (2020). Mo or W catalysts promoted with Ni or Co supported on modified bentonite for decane hydroconversion. *New Journal of Chemistry*, 44(7), 2966–2979. DOI: 10.1039/c9nj04878b.

[27] Priecel, P., Kubička, D., Vázquez-Zavala, A., Antonio de los Reyes, J., Pouzar, M., Čapek, L. (2020). Alternative Preparation of Improved NiMo-Alumina Deoxygenation Catalysts. *Frontiers in Chemistry*, 8(April), 1–12. DOI: 10.3389/fchem.2020.00216.

[28] Aryee, E., Dalai, A.K., Adjaye, J. (2021). Synthesis and Characterization of NiMo Catalysts Supported on Fine Carbon Particles for Hydrotreating: Effects of Metal Loadings in Catalyst Formulation. Frontiers in Chemical Engineering, 3(January), 1–14. DOI: 10.3389/fceng.2021.764931.

[29] Yang, J.K., Zuo, T.J., Lu, Y.Y., Zeng, W.S., Lu, J.Y. (2019). Catalytic performance of NiMo/Al2O3-USY in the hydrocracking of low-temperature coal tar. *Ranliao Huaxue Xuebao/Journal of Fuel Chemistry and Technology*, 47(9), 1053–1066. DOI: 10.1016/s1872-5813(19)30043-x.

[30] Fernández-Vargas, C., Ramírez, J., Gutiérrez-Alejandre, A., Sánchez-Minero, F., Cuevas-García, R., Torres-Mancera, P. (2008). Synthesis, characterization and evaluation of NiMo/SiO2-Al2O3 catalysts prepared by the pH-swing method. *Catalysis Today*, 130(2–4), 337–344. DOI: 10.1016/j.cattod.2007.10.101.

[31] Leyva, C., Rana, M.S., Ancheyta, J. (2008). Surface characterization of Al2O3-SiO2 supported NiMo catalysts: An effect of support composition. *Catalysis Today*, 130(2–4), 345–353. DOI: 10.1016/j.cattod.2007.10.113.

[32] Al-Dalama, K., Stanislaus, A. (2011). Temperature programmed reduction of SiO2-Al2O 3 supported Ni, Mo and NiMo catalysts prepared with EDTA. *Thermochimica Acta*, 520(1–2), 67–74. DOI: 10.1016/j.tca.2011.03.017.

[33] Fanani, Z., Asri, W.R., Dwiyanti, B., Rinaldi, N., Maryana, R., Muttaqii, M. Al, Riyanti, F., Mara, A., Zainul, R., Hasanudin, H. (2024). Efficient Catalytic Hydrocracking of Crude Palm Oil Over EDTA Template-assisted SiO2-Al2O3/ NiMo Catalysts. *Periodica Polytechnica Chemical Engineering*, 68(4), 552–560.

[34] Hosseinpour, N., Khodadadi, A.A., Mortazavi, Y., Bazyari, A. (2009). Nano-ceria-zirconia promoter effects on enhanced coke combustion and oxidation of CO formed in regeneration of silica-alumina coked during cracking of triisopropylbenzene. *Applied Catalysis A: General*, 353(2), 271–281. DOI: 10.1016/j.apcata.2008.10.051.

[35] Hamidi, R., Khoshbin, R., Karimzadeh, R. (2021). A new approach for synthesis of well-crystallized Y zeolite from bentonite and rice husk ash used in Ni-Mo/Al2O3-Y hybrid nanocatalyst for hydrocracking of heavy oil. *Advanced Powder Technology*, 32(2), 524–534. DOI: 10.1016/j.apt.2020.12.029.

[36] Oudghiri-Hassani, H., Al Wadaani, F. (2018). Preparation, Characterization and Catalytic Activity of Nickel Molybdate (NiMoO4) Nanoparticles. *Molecules*, 23, 273. DOI: 10.3390/molecules23020273.

[37] Majewski, A.J., Wood, J., Bujalski, W. (2013). Nickel-silica core@shell catalyst for methane reforming. *International Journal of Hydrogen Energy*, 38(34), 14531–14541. DOI: 10.1016/j.ijhydene.2013.09.017.

[38] Ando, M.F., Benzine, O., Pan, Z., Garden, J., Wondraczek, K., Grimm, S., Schuster, K., Wondraczek, L. (2018). Boson peak , heterogeneity and intermediate-range order in binary SiO2-Al2O3 glasses. *Scientific Reports*, 8, 5394. DOI: 10.1038/s41598-018-23574-1.

[39] Jothi Ramalingam, R., Appaturi, J.N., Pulingam, T., Al-Lohedan, H.A., Al-dhayan, D.M. (2020). In-situ incorporation of ruthenium/copper nanoparticles in mesoporous silica derived from rice husk ash for catalytic acetylation of glycerol. *Renewable Energy*, 160, 564–574. DOI: 10.1016/j.renene.2020.06.095.

[40] Gobara, H.M., Hassan, S.A., Betiha, M.A. (2016). The interaction characteristics controlling dispersion mode-catalytic functionality relationship of silica–modified montmorillonite-anchored Ni nanoparticles in petrochemical processes. *Materials Chemistry and Physics*, 181, 476–486. DOI: 10.1016/j.matchemphys.2016.06.084.

[41] Cornac, M., Janin, A., Lavalley, J.C. (1984). Application of FTIR spectroscopy to the study of sulfidation of Mo catalysts supported on alumina or silica (4000–400 cm^{-1} range). *Infrared Physics*, 24(2), 143–150. DOI: 10.1016/0020-0891(84)90062-9.

[42] Wachs, I.E. (1996). Raman and IR studies of surface metal oxide species on oxide supports: Supported metal oxide catalysts. *Catalysis Today*, 27(3–4), 437–455. DOI: 10.1016/0920-5861(95)00203-0.

[43] Topsoe, N.Y., Topsoe, H. (1993). FTIR Studies of Mo/Al2O3-Based Catalysts: I. Morphology and Structure of Calcined and Sulfided Catalysts. *Journal of Catalysis*, 139(2), 631–640. DOI: 10.1006/jcat.1993.1055.

[44] Morales Hernández, G., Escobar, J., Pacheco Sosa, J.G., Guzmán Cruz, M.A., Torres Torres, J.G., del Ángel Vicente, P., Barrera, M.C., Santolalla Vargas, C.E., Pérez Vidal, H. (2024). La-Modified SBA-15 Prepared by Direct Synthesis: Importance of Determining Actual Composition. *Catalysts*, 14(7), 1–13. DOI: 10.3390/catal14070436.

[45] Jafarian, S., Tavasoli, A., Nikkhah, H. (2019). Catalytic hydrotreating of pyro-oil derived from green microalgae spirulina the (Arthrospira) plantensis over NiMo catalysts impregnated over a novel hybrid support. *International Journal of Hydrogen Energy*, 44(36), 19855–19867. DOI: 10.1016/j.ijhydene.2019.05.182.

[46] Yu, X., Liu, B., Zhang, Y. (2019). Effect of Si/Al ratio of high-silica HZSM-5 catalysts on the prins condensation of isobutylene and formaldehyde to isoprene. *Heliyon*, 5(5), e01640. DOI: 10.1016/j.heliyon.2019.e01640.

[47] Wu, J., Zhu, H., Wu, Z., Qin, Z., Yan, L., Du, B., Fan, W., Wang, J. (2015). High Si/Al ratio HZSM-5 zeolite: An efficient catalyst for the synthesis of polyoxymethylene dimethyl ethers from dimethoxymethane and trioxymethylene. *Green Chemistry*, 17(4), 2353–2357. DOI: 10.1039/c4gc02510e.

[48] Korde, A., Min, B., Almas, Q., Chiang, Y., Nair, S., Jones, C.W. (2019). Effect of Si/Al Ratio on the Catalytic Activity of Two-Dimensional MFI Nanosheets in Aromatic Alkylation and Alcohol Etherification. *ChemCatChem*, 11(18), 4548–4557. DOI: 10.1002/cctc.201901042.

[49] Lü, J., Zhou, S., Ma, K., Meng, M., Tian, Y. (2015). The effect of P modification on the acidity of HZSM-5 and P-HZSM-5/CuO-ZnO-Al2O3 mixed catalysts for hydrogen production by dimethyl ether steam reforming. *Chinese Journal of Catalysis*, 36(8), 1295–1303. DOI: 10.1016/S1872-2067(15)60883-X.

[50] Yang, X., Liu, J., Fan, K., Rong, L. (2017). Hydrocracking of Jatropha Oil over non-sulfided PTA-NiMo/ZSM-5 Catalyst. *Scientific Reports*, 7(January), 1–14. DOI: 10.1038/srep41654.

[51] Vandevyvere, T., Sabbe, M.K., Mendes, P.S.F., Thybaut, J.W., Lauwaert, J. (2023). NiCu-based catalysts for the low-temperature hydrodeoxygenation of anisole: Effect of the metal ratio on SiO2 and γ-Al2O3 supports. *Green Carbon*, 1(2), 170–184. DOI: 10.1016/j.greenca.2023.10.001.

[52] Asri, W.R., Hasanudin, H., Wijaya, K. (2024). Highly Active Mesoporous Zirconium Nitride Immobilized on SiO2 Synthesized by Complex-Assisted Method with EDTA and KHP for Catalytic Hydroconversion of Crude Palm Oil. *Catalysis Surveys from Asia*, 28, 74–87. DOI: 10.1007/s10563-023-09413-y.

[53] Gustavo, F., Silveira, H., Villarroel-rocha, J., Sapag, K., Berenice, S., Gabriella, A., Santos, D. (2024). Al/SBA-15 Mesoporous Material: A Study of pH Influence over Aluminum Insertion into the Framework. *Nanomaterials*, 14(2). DOI: 10.3390/nano14020208.

[54] Putri, Q.U., Hasanudin, H., Asri, W.R. (2023). Production of levulinic acid from glucose using nickel phosphate - silica catalyst. *Reaction Kinetics, Mechanisms and Catalysis*, 136(1), 287–309. DOI: 10.1007/s11144-022-02334-3.

[55] Shimura, K., Yoshida, S., Oikawa, H., Fujitani, T. (2022). Ethylene oligomerization over NiOx/SiO2-Al2O3 catalysts prepared by a coprecipitation method. *Molecular Catalysis*, 528, 112478. DOI: 10.1016/j.mcat.2022.112478.

[56] Zhang, J., Chen, T., Jiao, Y., Cheng, M., Wang, L.L., Wang, J.L., Li, X.Y., Chen, Y.Q. (2021). Improved activity of Ni–Mo/SiO2 bimetallic catalyst synthesized via sol-gel method for methylcyclohexane cracking. *Petroleum Science*, 18(5), 1530–1542. DOI: 10.1016/j.petsci.2021.08.009.

[57] Liu, Y., Pan, C., Zou, Y., Wu, F., You, Z., Li, J. (2023). Nano-Fe/SiO2 catalysts prepared by facile colloidal deposition: Enhanced durability in Fischer-Tropsch synthesis. *Fuel*, 333(P2), 126514. DOI: 10.1016/j.fuel.2022.126514.

[58] Kaplin, I.Y., Lokteva, E.S., Golubina, E.V., Lunin, V.V. (2020). Template synthesis of porous ceria-based catalysts for environmental application. *Molecules*, 25(18) DOI: 10.3390/molecules25184242.

[59] Lenhardt, K.R., Breitzke, H., Buntkowsky, G., Reimhult, E., Willinger, M., Rennert, T. (2021). Synthesis of short-range ordered aluminosilicates at ambient conditions. *Scientific Reports*, 11(1), 1–13. DOI: 10.1038/s41598-021-83643-w.

[60] Hensen, E.J.M., Poduval, D.G., Magusin, P.C.M.M., Coumans, A.E., Veen, J.A.R. va. (2010). Formation of acid sites in amorphous silica-alumina. *Journal of Catalysis*, 269(1), 201–218. DOI: 10.1016/j.jcat.2009.11.008.

[61] Kumar, P., Maity, S.K., Shee, D. (2019). Role of NiMo Alloy and Ni Species in the Performance of NiMo/Alumina Catalysts for Hydrodeoxygenation of Stearic Acid: A Kinetic Study. *ACS Omega*, 4(2), 2833–2843. DOI: 10.1021/acsomega.8b03592.

[62] Subsadsana, M., Sansuk, S., Ruangviriyachai, C. (2018). Enhanced liquid biofuel production from crude palm oil over synthesized NiMoW-ZSM-5/MCM-41 catalyst. *Energy Sources, Part A: Recovery, Utilization and Environmental Effects*, 40(2), 237–243. DOI: 10.1080/15567036.2017.1411992.